ACS APPLIED MATERIALS & INTERFACES

www.acsami.org

Research Article

Self-Assembly of $CsPbBr_3$ Nanocubes into 2D Nanosheets

Qingye Zhang,[‖] Feiyu Diao,*[,‖] Xuyan Xue, Xiaoli Sheng, David Barba,* and Yiqian Wang*

Cite This: *ACS Appl. Mater. Interfaces* 2021, 13, 44777−44785

Read Online

ACCESS | Metrics & More | Article Recommendations | Supporting Information

ABSTRACT: All-inorganic metal halide perovskites have attracted considerable attention due to their high application potentials in optoelectronics, photonics, and energy conversion. Herein, two-dimensional (2D) $CsPbBr_3$ nanosheets with a thickness of about 3 nm have been synthesized through a simple chemical process based on a hot-injection technique. The lateral dimension of $CsPbBr_3$ nanosheets ranges from 11 to 110 nm, which can be tuned by adjusting the ratio of short ligands (octanoic acid and octylamine) over long ligands (oleic acid and oleylamine). The nanosheets result from the self-assembly of $CsPbBr_3$ nanocubes with an edge length of about 3 nm, which possess the same crystal orientation. In addition, an amorphous region of about 1 nm in width is found between adjacent nanocubes. To investigate both the structure and the growth mechanism of these nanosheets, microstructural characterizations at the atomic scale are conducted, combined with X-ray diffraction analysis, ^{1}H nuclear magnetic resonance (^{1}H NMR) measurement, and density functional theory (DFT) calculation, aiming to determine the configuration of different ligands adsorbed onto $CsPbBr_3$. Our results suggest that the adjacent nanocubes are mainly connected together by short ligands and inclined long ligands. On the basis of the DFT calculation results, a relationship is derived for the volume ratio of short ligands over long ligands and the lateral dimensions of $CsPbBr_3$ nanosheets. Moreover, a physicochemical mechanism is proposed to explain the 2D growth of $CsPbBr_3$ nanosheets. Such a finding provides new insights regarding the well-ordered self-arrangement of $CsPbBr_3$ nanomaterials, as well as new routes to synthesize 2D $CsPbX_3$ (X = Cl and I) nanosheets of suitable dimensions for specific and large-scale applications.

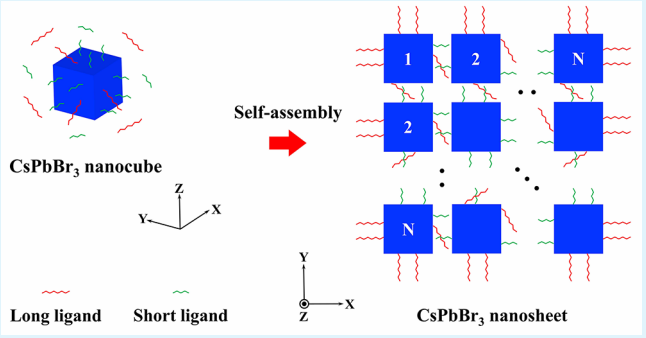

KEYWORDS: *$CsPbBr_3$ nanosheets, hot-injection, microstructure, formation mechanism, self-assembly*

INTRODUCTION

All-inorganic $CsPbX_3$ (X = Cl, Br, and I) nanomaterials have attracted specific attention because of their high light absorptivity, narrow photoluminescence (PL) emission, and high PL quantum yield (PLQY).[1−5] The physicochemical properties of these nanomaterials strongly depend on their size, shape, and composition.[6−15] For example, the bandgap of $CsPbX_3$ nanocubes can be controlled by adjusting their size,[16] and their PL emission spectra can be tuned by introducing different halide anions.[2] As compared to the nanocubes, two-dimensional (2D) $CsPbX_3$ nanosheets exhibit better optical nonlinearity,[17] larger exciton binding energy,[18] shorter PL decay time,[19,20] and lower stimulated emission threshold.[11]

Up to now, high-quality 2D $CsPbX_3$ nanosheets have been prepared using a reliable colloidal synthesis approach.[21] Liang et al.[11] fabricated 2D $CsPbBr_3$ nanosheets with an average lateral dimension of 75 nm and a thickness of 3 $CsPbBr_3$ perovskite unit cell layers by introducing oleic acid and octylamine ligands of a specific amount. Xiao et al.[22] synthesized $CsPbBr_3$ nanosheets with a thickness of 4.4 nm and an average lateral dimension of 30 nm by introducing additional metal bromides dissolved by oleic acid and oleylamine. Sun and co-workers[23] prepared $CsPbBr_3$ nanosheets with a typical thickness of 5.2 nm and an average lateral dimension of 100 nm by replacing hexanoic acid with oleic acid. Shamsi and co-workers[21] achieved control of the lateral dimension of $CsPbBr_3$ nanosheets by tuning the ratio of short ligands (octanoic acid and octylamine) over long ligands (oleic acid and oleylamine). In addition, Bekenstein et al.[24] synthesized 2D $CsPbBr_3$ nanosheets of 3 nm thickness, which originated from the attachment of single plates along specific directions. These reports demonstrated the critical effects induced by organic ligands on the lateral dimension of 2D $CsPbBr_3$ nanosheets. However, few studies paid attention to the fundamental dependence of the lateral dimension on organic ligands. Especially, the attachment of single plates resulting in 2D structures instead of three-dimensional (3D) structures still remains unclear. Such physical insight is

Received: July 1, 2021
Published: September 8, 2021

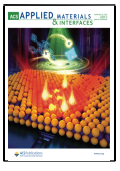

https://doi.org/10.1021/acsami.1c12247
ACS Appl. Mater. Interfaces 2021, 13, 44777−44785

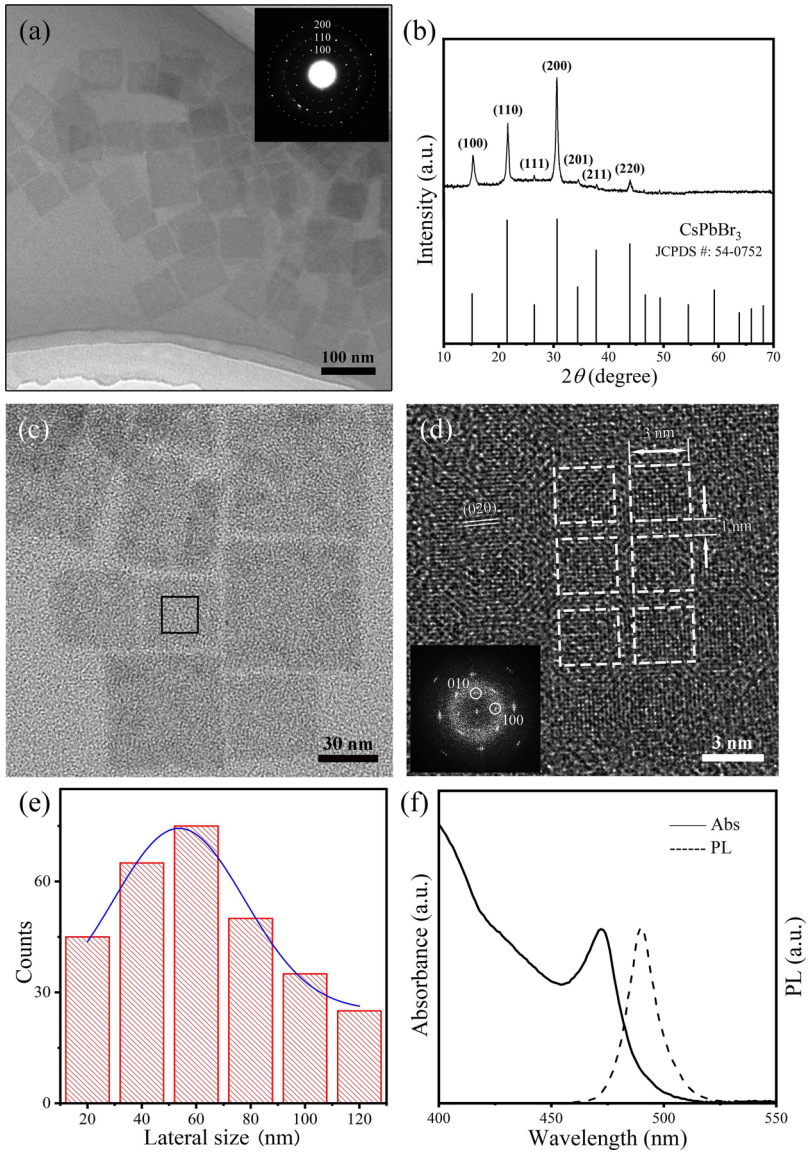

Figure 1. (a) Typical BF TEM image of the as-synthesized product. Inset is the corresponding SAED pattern. (b) XRD pattern of $CsPbBr_3$ nanosheets. (c) Enlarged BF TEM image of $CsPbBr_3$ nanosheets. (d) HRTEM image of the region enclosed by a black square in (c). Inset is the corresponding FFT pattern. (e) Statistical size distribution of $CsPbBr_3$ nanosheets. (f) Optical absorption (solid line) and PL emission (dash line) spectra of $CsPbBr_3$ nanosheets.

essential to design $CsPbBr_3$ nanosheets with a specific dimension and to develop efficient synthesis processes.

In this work, 2D $CsPbBr_3$ nanosheets with a uniform thickness of about 3 nm are prepared using a slightly adapted hot-injection approach. The lateral dimensions of the nanosheets are adjusted by controlling the volume ratio of short ligands over long ligands. The microstructures of the nanosheets are investigated by high-resolution transmission electron microscopy (HRTEM). These observations indicate that large 2D $CsPbBr_3$ nanosheets form through the self-assembly of 3 nm $CsPbBr_3$ nanocubes separated by an amorphous homogeneous region of 1 nm in width. ^{1}H NMR measurements and DFT calculations suggest the presence of short and long ligands between adjacent $CsPbBr_3$ nanocubes. A relationship is set up between the lateral dimension and the volume ratio of short ligands over long ligands. A reasonable self-assembly mechanism is proposed to describe the formation process of $CsPbBr_3$ nanosheets.

EXPERIMENTAL SECTION

Materials. The samples were prepared using the following chemical reagents: cesium carbonate (Cs_2CO_3, 99.9%, Aladdin), 1-octadecene (ODE, 90.0%, Aladdin), oleic acid (OlAc, 90.0%, Hushi), lead bromide ($PbBr_2$, 90.0%, Aladdin), oleylamine (OlAm, 90.0%, Aladdin), octanoic acid (OctAc, 90.0%, Hushi), octylamine (OctAm, 99.0%, Aladdin), and hexane (99.0%, Hushi). Each of them is used as received without further purification.

Methods. The 2D $CsPbBr_3$ nanosheets were prepared via the hot-injection method, according to the procedure described by Shamsi et al.,[21] by adding ODE into the mixture during the process of preparing cesium−oleate (Cs−oleate) solution.

For the preparation of cesium−oleate (Cs−oleate) solution, 0.2 g of Cs_2CO_3 was loaded into a three-neck flask of 100 mL along with 3 mL of OlAc and 5.1 mL of ODE. This mixture was stirred at 200 °C under N_2 flow until the complete dissolution of Cs_2CO_3, and then degassed under vacuum at 130 °C for 30 min. For further usage, the Cs−oleate solution was preheated at 100 °C.

To prepare $CsPbBr_3$ nanosheets, 10 mL of ODE and 0.145 g of $PbBr_2$ were loaded into a three-neck flask of 100 mL. Subsequently,

https://doi.org/10.1021/acsami.1c12247
ACS Appl. Mater. Interfaces 2021, 13, 44777−44785

long ligands (1 mL of OlAc and 1 mL of OlAm) and short ligands (0.325 mL of OctAc and 0.325 mL of OctAm) were added. The obtained mixture then was degassed under a vacuum at 120 °C for 1 h. After the complete dissolution of $PbBr_2$, the solution was heated to 130 °C under N_2 flow, and 0.9 mL of Cs−oleate solution was swiftly injected. After 5 s, the reaction mixture was cooled using an ice−water bath. Here, the volume ratio of short ligands over long ligands is defined as $R_{S/L}$. $R_{S/L}$ is adjusted by varying the volume of OctAc and OctAm from 0.18 to 0.45 mL to synthesize $CsPbBr_3$ nanosheets with different lateral dimensions.

To isolate and purify the synthesized products, the crude solution was centrifuged at 1000 rpm for 10 min. After centrifugation, the precipitation was discarded, and the supernatant was centrifuged at 3000 rpm for another 10 min. The supernatant was then discarded, and the precipitation was redispersed in 15 mL of hexane.

Characterization. The ultraviolet−visible (UV−vis) absorption spectra were recorded using a Persee TU-1901 double-beam spectrometer. To conduct the photoluminescence (PL) measurements, a Cary Eclipse fluorescence spectrophotometer was used. The X-ray diffraction (XRD) patterns were conducted on a Rigaku SmartLab apparatus using a Cu $K\alpha_1$ radiation source (λ = 1.5406 Å) with a step scan of 2° between 10° and 70°. The bright-field (BF) imaging, selected-area electron diffraction (SAED), and high-resolution TEM (HRTEM) examinations were performed using a JEOL JEM 2100F electron microscope operating at 200 kV. As the nanosheets were found to be sensitive to the electron beam exposure, all TEM images were recorded at a low beam current density of ∼15 pA/cm^2 to avoid any change induced by impinging electrons. Electron energy-loss spectroscopy (EELS) spectra were obtained on a JEOL JEM ARM200CF transmission electronic microscope, operating at 200 kV. The atomic force microscopy (AFM) examination was performed using a MFP-3D Origin atomic force microscope. The ^{1}H NMR patterns were recorded using a Bruker Avance III HD 400 MHz.

Computation Methods. All calculations were carried out using the CASTEP program package in Material Studio.[25] The Perdew−Burke−Ernzerhof (PBE) model of generalized gradient approximation (GGA) was used as the exchange-correlation function.[26] The ultrasoft pseudopotentials were used to treat the electron−ion interaction.[27,28] The convergence criteria of the energy, force, and displacement for optimized configuration were 5.0×10^{-6} eV per atom, 0.05 eV Å^{-1}, and 0.005 Å, respectively. An energy cutoff of 500 eV and a k-point mesh of $2\pi \times 0.03$ Å^{-1} were used. Periodic (3 × 3) slab models with one Br−Pb−Br or Pb−Br−Pb layer were created to represent the 2D nanosheets synthesized in the experiment, with the top and bottom surfaces being the Cs−Br or Pb−Br terminated (001) facets. The adsorption energy (E_{ads}) was calculated using the following equation:[29]

$$E_{ads} = E_{adsorbate} + E_{surface} - E_{adsorbate/surface} \quad (1)$$

where $E_{adsorbate/surface}$ is the total energy of the (001) surface of $CsPbBr_3$ with the adsorbed species, $E_{adsorbate}$ is the energy of the isolated adsorbed species in the vacuum, and $E_{surface}$ is the energy of the (001) surface of $CsPbBr_3$ without the adsorbed ligands. According to this equation, the positive value of E_{ads} means the adsorption configuration is thermodynamically stable and the stability of the adsorption configuration is positively correlated with E_{ads}.

RESULTS AND DISCUSSION

Microstructure of the Nanosheets. The size and morphology of the as-synthesized product were examined by TEM. Figure 1a shows a typical bright-field (BF) TEM image of the nanosheets synthesized with $R_{S/L}$ = 0.325. Their shapes are found to be roughly squared, with lateral dimensions varying from 30 to 100 nm. The thickness of the synthesized nanosheets is determined to be ∼3 nm by both AFM (Figures S1 and S2) and EELS (Figure S3) measurements. The SAED pattern of the synthesized nanosheets, displayed in the inset of Figure 1a, can be indexed using a cubic phase $CsPbBr_3$ (space group: $Pm\bar{3}m$, $a = b = c$ = 5.83 Å, $\alpha = \beta = \gamma = 90°$), showing three distinct diffraction rings, labeled as 100, 110, and 200. The XRD pattern of the nanosheets shows that the diffraction peaks at 15.2°, 21.6°, 26.5°, 30.6°, 34.4°, 37.8°, and 43.9° correspond to the {100}, {110}, {111}, {200}, {201}, {211}, and {220} crystal planes of cubic $CsPbBr_3$ (JCPDS no. 54-0752), respectively. Because the lateral dimension is much larger than the thickness of the nanosheets, four peaks corresponding to the {100}, {110}, {200}, and {220} planes exhibit higher intensity than the others, which is consistent with the SAED pattern shown in the inset of Figure 1a. A single peak located at ∼30° indicates that the $CsPbBr_3$ nanosheets do not belong to an orthorhombic phase.[30] No other crystal phase or impurity is detected.

To investigate the microstructure of the $CsPbBr_3$ nanosheets in detail, extensive HRTEM examinations were carried out. Figure 1c and d shows the enlarged BF TEM and HRTEM images of the $CsPbBr_3$ nanosheets. The HRTEM image displayed in Figure 1d is obtained from the region enclosed by a black square in Figure 1c. From Figure 1d, small nanocubes with an edge length of about 3 nm are observed, which are indicated by dashed lines. The lattice spacing of the small nanocubes is measured to be 2.92 Å, labeled by two parallel lines, which can be identified as the (020) plane of cubic $CsPbBr_3$. The fast Fourier transform (FFT) pattern presented in the inset of Figure 1d demonstrates that the nanosheet is single crystalline, in agreement with HRTEM observations. It is worth noting that an amorphous region with a width of around 1 nm is observed between two adjacent nanocubes. To display the amorphous regions more clearly, an enlarged HRTEM image of part of the $CsPbBr_3$ nanosheet is shown in Figure S4. Figure 1e shows the size-distribution of more than 300 $CsPbBr_3$ nanosheets observed by TEM. Their average dimension is found to be 55 nm, as obtained from the Gaussian fit of the size-distribution histogram. Figure 1f presents both the optical absorption (in solid line) and the PL emission (in dash line) spectra of the $CsPbBr_3$ nanosheets. As compared to the $CsPbBr_3$ nanocubes,[31] the absorption and PL emission peaks of $CsPbBr_3$ nanosheets are blue-shifted from 510 and 512 nm to 473 and 490 nm, respectively, which is attributed to the quantum confinement effect.[8]

Determination of the Amorphous Regions in the $CsPbBr_3$ Nanosheet. The amorphous region between two adjacent nanocubes (Figure 1d) is thought to be associated with the chemical ligands. To determine the type of ligands adsorbed on the surfaces of $CsPbBr_3$ nanocubes, ^{1}H NMR measurements were carried out. The investigations were conducted on dry $CsPbBr_3$ powders to avoid the decomposition of $CsPbBr_3$ caused by direct contact with water. Figure 2 shows the ^{1}H NMR patterns of pure OctAm, OlAm, OctAc, and OlAc ligands and of as-prepared $CsPbBr_3$ nanosheets. For pure OctAm, OlAm, OctAc, and OlAc, the peak at 2.50 ppm is related to the chemical shift of hydrogens (δ) in DMSO-d_6 solvent, and the peak at 3.35 ppm corresponds to water in DMSO-d_6.[32] For OlAm and OctAm, the peaks marked by asterisk (*) are located at 7.54 ppm, which corresponds to the amino proton ($-NH_3^+$).[33] The measurements recorded on $CsPbBr_3$ nanosheets reveal a shift from 7.54 to 7.69 ppm, indicating that amino protons from OlAm and OctAm ligands are bonded with Br^- ions in the $CsPbBr_3$.[34] In comparison with the ^{1}H NMR patterns of OlAc and OctAc, the peak marked by "▽" is slightly shifted from

https://doi.org/10.1021/acsami.1c12247
ACS Appl. Mater. Interfaces 2021, 13, 44777−44785

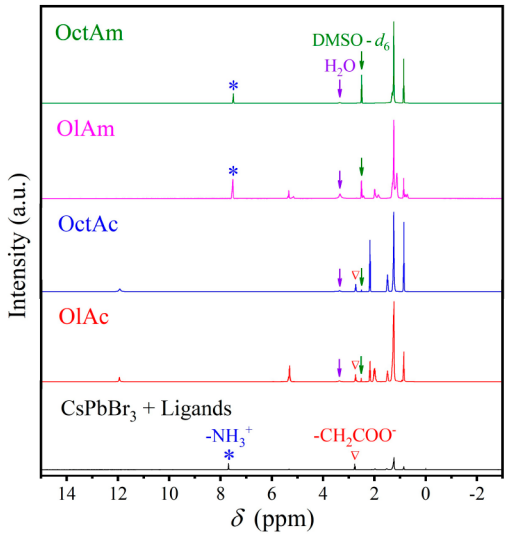

Figure 2. ^{1}H NMR spectra of pure OctAm, OlAm, OctAc, and OlAc ligands and of $CsPbBr_3$ nanosheets with ligands.

2.73 to 2.77 ppm, indicating that the carboxyls (COO^-) of the OlAc and OctAc ligands are bonded with the Cs^+ and Pb^{2+} ions in the $CsPbBr_3$,[34] which affects the chemical potential of the carboxyl protons ($-CH_2COO^-$). These results suggest that all of the chemical ligands of OlAc, OlAm, OctAc, and OctAm are adsorbed onto the surfaces of the $CsPbBr_3$ nanocubes.

The ^{1}H NMR results indicate the existence of both short and long ligands on the surfaces of the $CsPbBr_3$ nanosheets, but fail to distinguish the active sites of various ligands. Thus, the DFT calculations are performed to investigate the adsorption behaviors of OlAc, OlAm, OctAc, and OctAm onto the $CsPbBr_3$ (001) surfaces. The chain lengths of the OlAc, OlAm, OctAc, and OctAm molecules are calculated to be 24.34, 23.85, 10.96, and 11.02 Å, respectively. It can be found that the length of the short ligand is compatible with the 1 nm width of the amorphous region between the adjacent nanocubes observed in Figure 1d. Meanwhile, the long ligands tilted at a certain angle (≤30°) along the surface of the nanocubes also satisfy with the width of the amorphous regions. Figure S5 shows a schematic illustration of the amorphous region composed of a long ligand with a tilt angle of 30° and a short ligand perpendicular to the nanocube surface. Therefore, several adsorption configurations of different ligands including perpendicular long ligands, inclined long ligands, and perpendicular short ligands on $CsPbBr_3$ (001) surfaces are considered to clarify the ligand species in the amorphous regions. Figure 3 shows all of the optimized configurations of chemical ligands adsorbed on the Cs−Br terminated (001) surfaces, and Figure 4 presents the optimized configurations of chemical ligands adsorbed on the Pb−Br terminated surfaces. The corresponding adsorption energies are displayed in Table 1. From Table 1, it can be seen that positive adsorption energies are obtained for all of the configurations, confirming that both short and long ligands can adsorb on the $CsPbBr_3$ (001) surfaces, which is consistent with the ^{1}H NMR results. By further examining the calculated absorption energies, it can be found that amino ligands (i.e., OlAm and OctAm) are preferentially adsorbed on the Pb−Br terminated surfaces, while carboxylic ligands such as OlAc and OctAc are preferentially adsorbed on the Cs−Br terminated surfaces. In addition, for the Pb−Br terminated surfaces, the order of preferential adsorption for the chemical ligands is OctAm, inclined OlAm, and perpendicular OlAm. However, for the Cs−Br terminated surfaces, the order of preferential adsorption for the chemical ligands is OctAc, inclined OlAc, and perpendicular OlAc. In one word, the short ligands are preferentially adsorbed on $CsPbBr_3$ (001) surfaces as compared to the long ligands, and the inclined long ligands are more stable than the perpendicular ones when adsorbed on $CsPbBr_3$ (001) surfaces. Accordingly, it can be inferred that both short ligands (OctAm and OctAc) and inclined long ligands (OlAm and OlAc) are dominated to locate in the amorphous regions between the adjacent $CsPbBr_3$ nanocubes, while perpendicular long ligands are mainly adsorbed on the exposed surfaces of the nanosheets.

Geometric Configuration of the $CsPbBr_3$ Nanosheet. On the basis of the results of DFT calculations, a theoretical

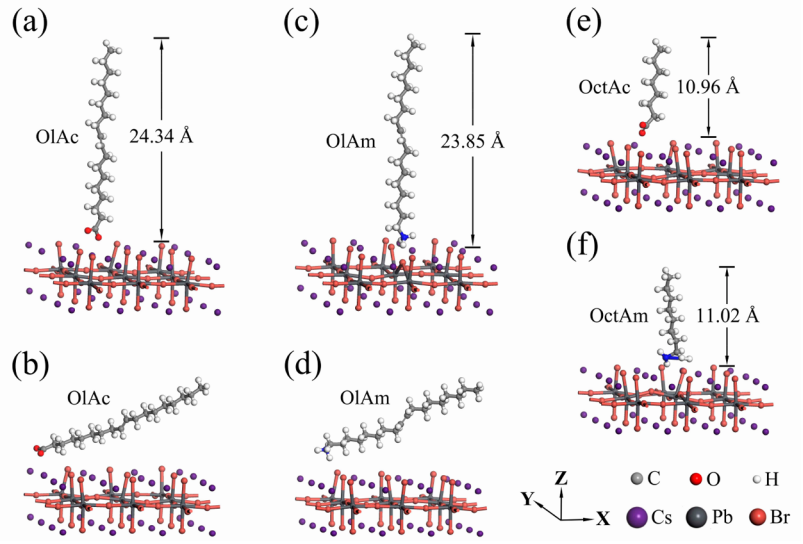

Figure 3. Adsorption configuration of ligands on Cs−Br terminated $CsPbBr_3$ (001) surfaces. (a) Perpendicular OlAc, (b) inclined OlAc, (c) perpendicular OlAm, (d) inclined OlAm, (e) perpendicular OctAc, and (f) perpendicular OctAm.

https://doi.org/10.1021/acsami.1c12247
ACS Appl. Mater. Interfaces 2021, 13, 44777−44785

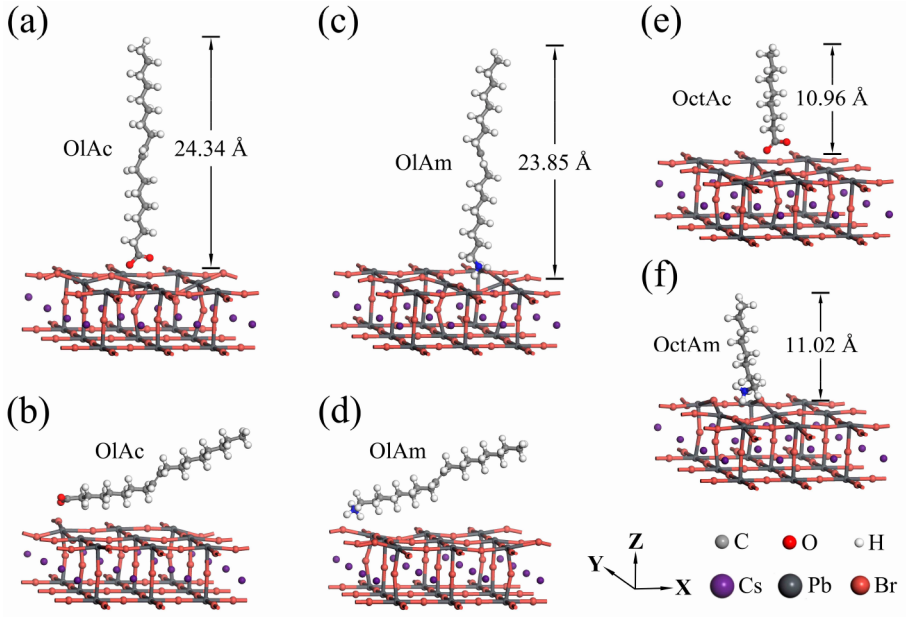

Figure 4. Adsorption configuration of ligands on Pb−Br terminated $CsPbBr_3$ (001) surfaces. (a) Perpendicular OlAc, (b) inclined OlAc, (c) perpendicular OlAm, (d) inclined OlAm, (e) perpendicular OctAc, and (f) perpendicular OctAm.

Table 1. Adsorption Energies of Ligands Adsorbed on Cs−Br and Pb−Br Terminated $CsPbBr_3$ (001) Surfaces

ligand	termination surface	configuration	E_{ads} (eV)
OlAc (long)	Cs−Br	inclined	0.870
		perpendicular	0.515
	Pb−Br	perpendicular	0.406
		inclined	0.024
OlAm (long)	Pb−Br	inclined	1.852
		perpendicular	1.658
	Cs−Br	perpendicular	1.285
		inclined	0.879
OctAc (short)	Cs−Br	perpendicular	0.966
	Pb−Br		0.494
OctAm (short)	Pb−Br	perpendicular	2.005
	Cs−Br		0.139

model for the geometric configuration of $CsPbBr_3$ nanosheet is built to disclose the relationship between the lateral size (L) and $R_{S/L}$. As shown in Figure 5, we hypothesize that there are

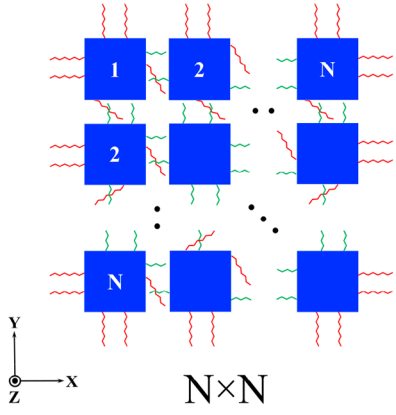

Figure 5. Schematic illustration of the geometric configuration of the $CsPbBr_3$ nanosheet.

$N \times N$ nanocubes in one nanosheet. Two ligands per nanocube face are assigned to make it easy to count the number of short and long ligands, respectively. Considering that long ligands serve as the capping agents, two perpendicular long ligands are located on the exposed surfaces of the nanocube. According to the DFT calculations, the amorphous region between adjacent nanocubes is composed of short ligands and inclined long ligands. Although the location of short and long ligands is clear, the number of short or inclined long ligands is uncertain in the amorphous regions. For one amorphous region, it is ascertained that there are no more than four ligands because of the steric hindrance. We then derive the mathematical formula to describe the relationship between the lateral size (L), the theoretical number of short ligands (N_{short}), the number of long ligands (N_{long}), and N as follows:

$$L = N \times 3 + (N - 1) \times 1 = 4N - 1 \tag{2}$$

$$N_{short} = 2 \times N \times (N - 1) \times x \tag{3}$$

$$N_{long} = 2 \times (N \times 4 + N^2 \times 2) + 2 \times N \times (N - 1) \times (N_{in} - x) \tag{4}$$

where N_{in} is the sum of the numbers of short and long ligands in an amorphous region, which is less than 4, and x is the number of short ligands. Accordingly, the theoretical volume ratio of short ligands over long ligands ($R_{T\text{-}S/L}$) is given as follows:

$$R_{T\text{-}S/L} = \frac{1}{2} \times \frac{N_{short}}{N_{long}} \tag{5}$$

To ascertain N_{in} and x, we discussed all possible models of the as-prepared nanosheet ($R_{S/L}$= 0.325, L = 55 nm, and N = 14) as listed in Table 2. It shows that the $R_{T\text{-}S/L}$ value (0.289) in the case of N_{in} = 3, x = 2 is nearest to the experimental one (0.325), meaning that two short ligands and one long ligand exist in the amorphous region between the adjacent $CsPbBr_3$ nanocubes, as illustrated in Figure 5.

https://doi.org/10.1021/acsami.1c12247
ACS Appl. Mater. Interfaces 2021, 13, 44777−44785

Table 2. Calculated $R_{T\text{-}S/L}$ Values of Different Models for the $CsPbBr_3$ Nanosheets with L = 55 nm and N = 14

models	N_{short}	N_{long}	N_{short}/N_{long}	$R_{T\text{-}S/L}$
N_{in} = 4, x = 4	1456	896	1.625	0.813
N_{in} = 4, x = 3	1092	1260	0.867	0.434
N_{in} = 4, x = 2	728	1624	0.448	0.224
N_{in} = 4, x = 1	364	2072	0.176	0.088
N_{in} = 3, x = 3	1092	896	1.219	0.609
N_{in} = 3, x = 2	728	1260	0.578	0.289
N_{in} = 3, x = 1	364	1624	0.224	0.112
N_{in} = 2, x = 2	728	896	0.813	0.407
N_{in} = 2, x = 1	364	1260	0.289	0.144
N_{in} = 1, x = 1	364	896	0.406	0.203

To verify this theoretical model, we adjusted $R_{S/L}$ to prepare the $CsPbBr_3$ nanosheets with different lateral sizes. The $CsPbBr_3$ nanosheets with average lateral sizes of 11, 15, 55, and 110 nm are produced with $R_{S/L}$ = 0.154, 0.21, 0.325, and 0.38, respectively. Figure 6a,b and c,d presents typical BF TEM and HRTEM images of $CsPbBr_3$ nanosheets produced with volume ratios of 0.21 and 0.38, respectively. The HRTEM images show that these nanosheets are also composed of many small nanocubes. The FFT patterns presented in the inset of Figure 6b and d clearly indicate that the nanosheet is single crystalline, in good agreement with HRTEM observations. Figure S6 shows the statistical lateral size distributions of the $CsPbBr_3$ nanosheets produced with $R_{S/L}$ = 0.21 and 0.38, showing an average lateral size of 15 and 110 nm, respectively. The XRD patterns show that all of the produced nanosheets are cubic perovskite $CsPbBr_3$. The XRD patterns of $CsPbBr_3$ nanosheets with a lateral size of 11 and 15 nm show more random orientation than that of the $CsPbBr_3$ nanosheets with a lateral size of 110 nm, which is ascribed to the fact that larger

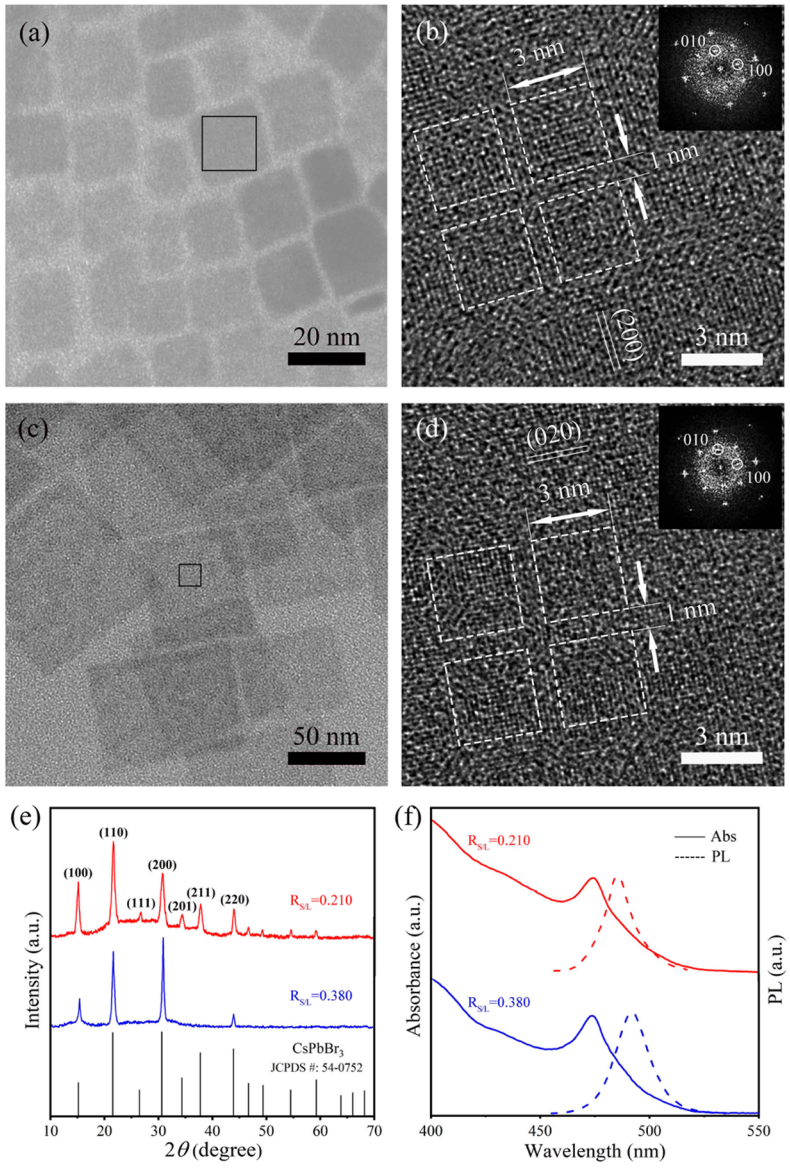

Figure 6. Typical BF TEM (a and c) and HRTEM images (b and d) of the $CsPbBr_3$ nanosheets produced with a volume ratio of 0.210 and 0.380, respectively. (e) Experimental XRD patterns of the corresponding $CsPbBr_3$ nanosheets along with the standard XRD pattern of cubic $CsPbBr_3$ (JCPDS no. 54-0752). (f) Optical absorption (solid line) and PL emission (dash line) spectra of the corresponding $CsPbBr_3$ nanosheets.

https://doi.org/10.1021/acsami.1c12247
ACS Appl. Mater. Interfaces 2021, 13, 44777−44785

nanosheets are more easily tiled on a flat surface. The absorption and PL emission peaks of the $CsPbBr_3$ nanosheets synthesized with $R_{S/L}$ = 0.154, 0.21, and 0.38 are also blue-shifted, which are analogous to the nanosheets synthesized with $R_{S/L}$ = 0.325. Figure S7 presents the corresponding measurements for $CsPbBr_3$ nanosheets with an average lateral size of 11 nm produced with $R_{S/L}$ = 0.154.

Similarly, we calculated the $R_{T\text{-}S/L}$ values for the $CsPbBr_3$ nanosheets with an average lateral size of 11, 15, 55, and 110 nm using eqs 3−6 with N_{in} = 3 and x = 2. The calculated results are displayed in Table 3. A considerable deviation is

Table 3. Calculated $R_{T\text{-}S/L}$ and $R^r_{T\text{-}S/L}$ Values of the $CsPbBr_3$ Nanosheets with Different Lateral Sizes

L (nm)	N	$R_{S/L}$	$R_{T\text{-}S/L}$	$R^r_{T\text{-}S/L}$
11	3	0.154	0.167	0.159
15	4	0.210	0.200	0.200
55	14	0.325	0.289	0.328
110	28	0.380	0.310	0.379

found between $R_{T\text{-}S/L}$ and $R_{S/L}$ except for the $CsPbBr_3$ nanosheets with an average lateral size of 15 nm. In other words, only when N = 4 is the theoretical $R_{T\text{-}S/L}$ value approximately equal to the experimental $R_{S/L}$ value. In addition, when N < 4, $R_{T\text{-}S/L}$ is more than $R_{S/L}$; when N > 4, $R_{T\text{-}S/L}$ is less than $R_{S/L}$. This can be explained by the fact that the steric hindrance in the $CsPbBr_3$ nanosheet increases with the expansion of its lateral size, which reduces the number of long ligands in the amorphous region between two adjacent nanocubes. Therefore, we define a coefficient of steric hindrance ($k = 1/\log(N, 4)$) to get N_{long} corrected as follows:

$$N_{long} = 2 \times (N \times 4 + N^2 \times 2) + 2 \times N \times (N - 1) \times k \quad (6)$$

We then can obtain the revised theoretical volume ratio ($R^r_{T\text{-}S/L}$) of short ligands over long ligands:

$$R^r_{T\text{-}S/L} = \frac{1}{2} \times \frac{N_{short}}{N_{long}} = \frac{1}{2} \times \frac{2 \times N \times (N - 1) \times 2}{2 \times (N \times 4 + N^2 \times 2) + 2 \times N \times (N - 1) \times k} \quad (7)$$

From Table 3, it can be seen the revised theoretical volume ratios are very close to the experimental ones. Now, the relation between L and $R_{S/L}$ is established through N, as shown in Figure 7. These results indicate that the geometric configurations in Figure 5 are in good accord with the real structure of the $CsPbBr_3$ nanosheet and are helpful to control the lateral size of the 2D $CsPbBr_3$ nanosheet.

2D Growth Mechanism of Nanosheets. On the basis of the above results, a possible formation mechanism of the $CsPbBr_3$ nanosheets is proposed, as shown in Figure 8. Figure 8a shows the 3D model of a formed $CsPbBr_3$ nanocube. In Figure 8b−f, the self-assembly process of nanocubes to nanosheet is presented from the top view, where the 2D arrangement of the nanocubes defines the horizontal x−y plane. At the initial stage of the reaction, a large amount of $CsPbBr_3$ nanocubes with an edge length of 3 nm form, which are packaged by different ligands including short and long ligands. According to the DFT calculations, the adsorbed ligands are dominated by short ligands and inclined long

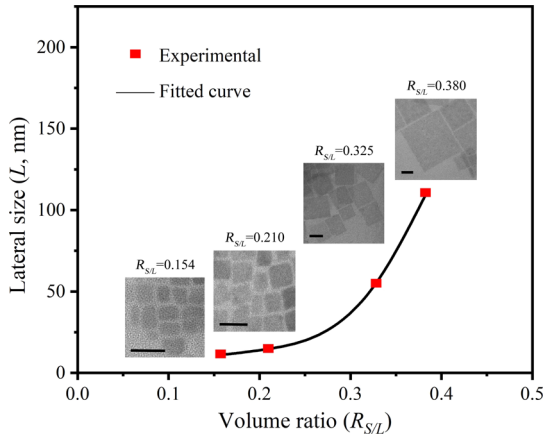

Figure 7. Evolution of the lateral size of $CsPbBr_3$ nanosheets upon the volume ratio $R_{S/L}$. Insets are BF TEM images of $CsPbBr_3$ nanosheets with different lateral sizes. (All of the scale bars represent 30 nm.)

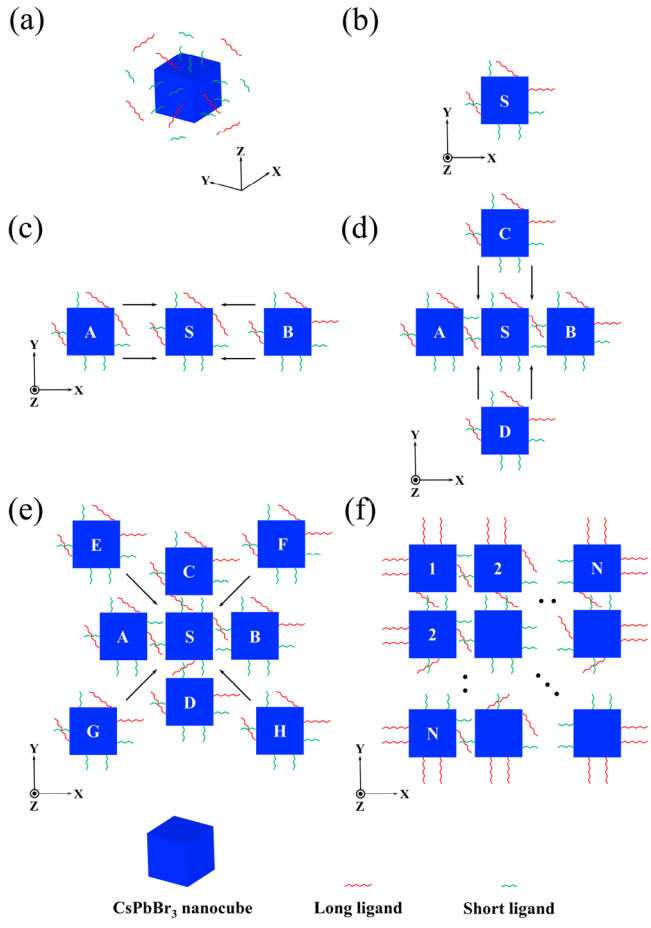

Figure 8. Schematic illustration of the formation mechanism for the $CsPbBr_3$ nanosheet. (a) $CsPbBr_3$ nanocube with adsorbed ligands, (b) top view of the $CsPbBr_3$ nanocube with adsorbed ligands, (c,d) formation of a pre-$CsPbBr_3$-nanosheet, and (e,f) 2D self-assembly of $CsPbBr_3$ nanocubes.

ligands and some perpendicular long ligands. Under the van der Waals interactions between nanocubes,[35] these small nanocubes tend to agglomerate together to form larger nanostructures. However, the ligands prevent the random agglomerations and guide the ordered self-assembly of

https://doi.org/10.1021/acsami.1c12247
ACS Appl. Mater. Interfaces 2021, 13, 44777−44785

nanocubes to 2D nanosheets. Here, we choose one $CsPbBr_3$ nanocube as the seed of a nanosheet (labeled S in Figure 8b) to explain the epitaxial growth. In the early stage of the self-assembly process, oriented attachment of nanoparticles takes place predominantly in one direction to decrease the overall energy of system.[36] Therefore, in the first step of the 2D growth (Figure 8c), nanocubes A and B attach to S from the horizontal direction and are stabilized by short ligands and inclined long ligands. During this process, the perpendicular long ligands adsorbed onto two linking surfaces of nanocubes S and A (and B) would desorb or turn to inclined adsorption under the pressure between nanocubes. Because of the energy minimization principle of the system, the attachment of the latter nanocubes (C and D) takes place from the vertical direction, as shown in Figure 8d. So far, a preliminary anisotropic 2D $CsPbBr_3$ nanosheet (pre-$CsPbBr_3$-nanosheet) forms. The top and bottom surfaces along the *z*-axis accommodate a great number of perpendicular long ligands, which act as inhibitors of the growth along the *z*-axis. Subsequently, the nanocubes E, F, G, and H attach to the pre-$CsPbBr_3$-nanosheet diagonally, which promotes the 2D growth of $CsPbBr_3$, as depicted in Figure 8e and f. The self-assembly process will stop with the depletion of the ligands around the formed $CsPbBr_3$ nanosheet.

From the foregoing, it is reasonable to conclude that the self-assembly of $CsPbBr_3$ nanocubes takes place only along the horizontal *x*−*y* plane, which is motivated by the van der Waals interactions between nanocubes and the energy minimization principle of the system. In addition, the assembly of $CsPbBr_3$ nanocubes along *z*-axis is hindered by the long ligands perpendicular to the top and bottom surfaces of nanocubes. The formation mechanism of the $CsPbBr_3$ nanosheets is similar to that of the ultrathin PbS sheets.[37,38]

CONCLUSIONS

In this work, 2D $CsPbBr_3$ nanosheets with a thickness of about 3 nm have been synthesized using a simple method based on the hot-injection technique. The lateral dimension of the nanosheets can be tuned by adjusting the ratio of short ligands (octanoic acid and octylamine) over long ligands (oleic acid and oleylamine). The $CsPbBr_3$ nanosheets consist of many $CsPbBr_3$ nanocubes with an edge length of 3 nm. The DFT calculations of the $CsPbBr_3$ surfaces terminated by Pb−Br or Cs−Br layers reveal that the nanocubes are connected together through short ligands and inclined long ligands, forming an intermediate amorphous layer of 1 nm in width. In addition, the predominant adsorption of perpendicular long ligands onto the top and bottom faces of the nanosheets prevents the assembly of nanocubes along the direction perpendicular to the nanosheet plane. Our work can deepen the understanding of the formation mechanism for the 2D $CsPbX_3$ (X = Cl, Br, I) nanosheets.

ASSOCIATED CONTENT

Supporting Information

The Supporting Information is available free of charge at https://pubs.acs.org/doi/10.1021/acsami.1c12247.

Additional information including AFM examination of $CsPbBr_3$ nanosheets; statistical thickness distributions of $CsPbBr_3$ nanosheets; EELS measurements of $CsPbBr_3$ nanosheet; enlarged HRTEM image of $CsPbBr_3$ nanosheet; schematic illustration of the geometric configuration of adsorbed ligands; statistical lateral size distributions of $CsPbBr_3$ nanosheets; and BF TEM image, XRD pattern, statistical lateral size distribution, optical absorption, and PL emission spectra of $CsPbBr_3$ nanosheets (PDF)

AUTHOR INFORMATION

Corresponding Authors

Feiyu Diao − *Industrial Research Institute of Nonwovens & Technical Textiles, College of Textiles & Clothing, Qingdao University, Qingdao 266017, People's Republic of China*; Email: fydiao@qdu.edu.cn

David Barba − *Centre Énergie Matériaux et Télécommunications, Institut National de la Recherche Scientifique, Varennes, Québec J3X 1S2, Canada*; Email: barba@emt.inrs.ca

Yiqian Wang − *College of Physics, Qingdao University, Qingdao 266017, People's Republic of China*; orcid.org/0000-0003-3341-7614; Email: yqwang@qdu.edu.cn

Authors

Qingye Zhang − *College of Physics, Qingdao University, Qingdao 266017, People's Republic of China*

Xuyan Xue − *College of Physics, Qingdao University, Qingdao 266017, People's Republic of China*

Xiaoli Sheng − *College of Physics, Qingdao University, Qingdao 266017, People's Republic of China*

Complete contact information is available at: https://pubs.acs.org/10.1021/acsami.1c12247

Author Contributions

‖Q.Z. and F.D. contributed equally to this work.

Notes

The authors declare no competing financial interest.

ACKNOWLEDGMENTS

We are thankful for financial support from the High-end Foreign Experts Recruitment Programs (grant nos. GDW20173500154 and GDW20163500110), the Shandong Province "Double-Hundred Talent Plan" (grant no. WST2018006), the Shandong Province High-end Foreign Experts Recruitment Program, and the Top-notch Innovative Talent Program of Qingdao City, China (grant no. 13-CX-8). Y.W. is also thankful for financial support from the Taishan Scholar Program of Shandong Province, China, the Qingdao International Center of Semiconductor Photoelectric Nanomaterials, and the Shandong Provincial University Key Laboratory of Optoelectrical Material Physics and Devices.

REFERENCES

(1) Swarnkar, A.; Chulliyil, R.; Ravi, V. K.; Irfanullah, M.; Chowdhury, A.; Nag, A. Colloidal $CsPbBr_3$ Perovskite Nanocrystals: Luminescence beyond Traditional Quantum Dots. *Angew. Chem., Int. Ed.* **2015**, *54*, 15424−15428.

(2) Nedelcu, G.; Protesescu, L.; Yakunin, S.; Bodnarchuk, M. I.; Grotevent, M. J.; Kovalenko, M. V. Fast Anion-Exchange in Highly Luminescent Nanocrystals of Cesium Lead Halide Perovskites ($CsPbX_3$, X = Cl, Br, I). *Nano Lett.* **2015**, *15*, 5635−5640.

(3) Wu, K. F.; Liang, G. J.; Shang, Q. Y.; Ren, Y. P.; Kong, D. G.; Lian, T. Q. Ultrafast Interfacial Electron and Hole Transfer from $CsPbBr_3$ Perovskite Quantum Dots. *J. Am. Chem. Soc.* **2015**, *137*, 12792−12795.

(4) Akkerman, Q. A.; D'Innocenzo, V.; Accornero, S.; Scarpellini, A.; Petrozza, A.; Prato, M.; Manna, L. Tuning the Optical Properties of Cesium Lead Halide Perovskite Nanocrystals by Anion Exchange Reactions. *J. Am. Chem. Soc.* **2015**, *137*, 10276−10281.
(5) Kim, Y.; Yassitepe, E.; Voznyy, O.; Comin, R.; Walters, G.; Gong, X. W.; Kanjanaboos, P.; Nogueira, A. F.; Sargent, E. H. Efficient Luminescence from Perovskite Quantum Dot Solids. *ACS Appl. Mater. Interfaces* **2015**, *7*, 25007−25013.
(6) Cai, J. J.; Yan, C.; Luo, C.; Li, W.; Zeng, X. K.; Xu, Z.; Fu, X. H.; Wang, Q.; Chu, X.; Huang, H. C.; Zhao, X. Y.; Lu, J.; Yang, W. Q. Cryogenic-Temperature Thermodynamically Suppressed and Strongly Confined $CsPbBr_3$ Quantum Dots for Deeply Blue Light-Emitting Diodes. *Adv. Opt. Mater.* **2021**, *9*, 2100300.
(7) Burda, C.; Chen, X. B.; Narayanan, R.; Ei-Sayed, M. A. Chemistry and Properties of Nanocrystals of Different Shapes. *Chem. Rev.* **2005**, *105*, 1025−1102.
(8) Butkus, J.; Vashishtha, P.; Chen, K.; Gallaher, J. K.; Prasad, S. K. K.; Metin, D. Z.; Laufersky, G.; Gaston, N.; Halpert, J. E.; Hodgkiss, J. M. The Evolution of Quantum Confinement in $CsPbBr_3$ Perovskite Nanocrystals. *Chem. Mater.* **2017**, *29*, 3644−3652.
(9) Mokari, T.; Zhang, M. J.; Yang, P. D. Shape, Size, and Assembly Control of PbTe Nanocrystals. *J. Am. Chem. Soc.* **2007**, *129*, 9864−9865.
(10) Li, Z. J.; Hofman, E.; Davis, A. H.; Maye, M. M.; Zheng, W. W. General Strategy for the Growth of $CsPbX_3$ (X = Cl, Br, I) Perovskite Nanosheets from the Assembly of Nanorods. *Chem. Mater.* **2018**, *30*, 3854−3860.
(11) Liang, Z. Q.; Zhao, S. L.; Xu, Z.; Qiao, B.; Song, P. J.; Gao, D.; Xu, X. R. Shape-Controlled Synthesis of All-Inorganic $CsPbBr_3$ Perovskite Nanocrystals with Bright Blue Emission. *ACS Appl. Mater. Interfaces* **2016**, *8*, 28824−28830.
(12) Wang, C.; Wang, Y. Q.; Liu, X. H.; Yang, H. W.; Sun, J. R.; Yuan, L.; Zhou, G. W.; Rosei, F. Structure Versus Properties in α-Fe_2O_3 Nanowires and Nanoblades. *Nanotechnology* **2016**, *27*, 035702.
(13) Zhu, P. C.; Zhu, J. Low-Dimensional Metal Halide Perovskites and Related Optoelectronic Applications. *InfoMat* **2020**, *2*, 341−378.
(14) Zheng, Z.; Hu, Q. S.; Zhou, H. Z.; Luo, P.; Nie, A. M.; Zhu, H. M.; Gan, L.; Zhuge, F. W.; Ma, Y.; Song, H. S.; Zhai, T. Y. Submillimeter and Lead-Free $Cs_3Sb_2Br_9$ Perovskite Nanoflakes: Inverse Temperature Crystallization Growth and Application for Ultrasensitive Photodetectors. *Nanoscale Horiz.* **2019**, *4*, 1372−1379.
(15) Guo, Y. J.; Su, J.; Wang, L.; Lin, Z. H.; Hao, Y.; Chang, J. J. Improved Doping and Optoelectronic Properties of Zn-Doped $CsPbBr_3$ Perovskite through Mn Codoping Approach. *J. Phys. Chem. Lett.* **2021**, *12*, 3393−3400.
(16) Maes, J.; Balcaen, L.; Drijvers, E.; Zhao, Q.; De Roo, J.; Vantomme, A.; Vanhaecke, F.; Geiregat, P.; Hens, Z. Light Absorption Coefficient of $CsPbBr_3$ Perovskite Nanocrystals. *J. Phys. Chem. Lett.* **2018**, *9*, 3093−3097.
(17) Yang, Z.; Wang, M. Q.; Qiu, H. W.; Yao, X.; Lao, X. Z.; Xu, S. J.; Lin, Z. H.; Sun, L. Y.; Shao, J. Y. Engineering the Exciton Dissociation in Quantum-Confined 2D $CsPbBr_3$ Nanosheet Films. *Adv. Funct. Mater.* **2018**, *28*, 1705908.
(18) Jin, B.; Zuo, N.; Hu, Z. Y.; Cui, W. J.; Wang, R. Y.; Van Tendeloo, G.; Zhou, X.; Zhai, T. Y. Excellent Excitonic Photovoltaic Effect in 2D $CsPbBr_3$/CdS Heterostructures. *Adv. Funct. Mater.* **2020**, *30*, 2006166.
(19) Li, X. M.; Wu, Y.; Zhang, S. L.; Cai, B.; Gu, Y.; Song, J. Z.; Zeng, H. B. $CsPbX_3$ Quantum Dots for Lighting and Displays: Room-Temperature Synthesis, Photoluminescence Superiorities, Underlying Origins and White Light-Emitting Diodes. *Adv. Funct. Mater.* **2016**, *26*, 2435−2445.
(20) Li, J.; Luo, L. H.; Huang, H. W.; Ma, C.; Ye, Z. Z.; Zeng, J.; He, H. P. 2D Behaviors of Excitons in Cesium Lead Halide Perovskite Nanoplatelets. *J. Phys. Chem. Lett.* **2017**, *8*, 1161−1168.
(21) Shamsi, J.; Dang, Z. Y.; Bianchini, P.; Canale, C.; Di Stasio, F.; Brescia, R.; Prato, M.; Manna, L. Colloidal Synthesis of Quantum Confined Single Crystal $CsPbBr_3$ Nanosheets with Lateral Size Control up to the Micrometer Range. *J. Am. Chem. Soc.* **2016**, *138*, 7240−7243.
(22) Xiao, X. L.; Li, Y.; Xie, R. J. Blue-Emitting and Self-Assembled Thinner Perovskite $CsPbBr_3$ Nanoplates: Synthesis and Formation Mechanism. *Nanoscale* **2020**, *12*, 9231−9239.
(23) Sun, S. B.; Yuan, D.; Xu, Y.; Wang, A. F.; Deng, Z. T. Ligand-Mediated Synthesis of Shape-Controlled Cesium Lead Halide Perovskite Nanocrystals *via* Reprecipitation Process at Room Temperature. *ACS Nano* **2016**, *10*, 3648−3657.
(24) Bekenstein, Y.; Koscher, B. A.; Eaton, S. W.; Yang, P. D.; Alivisatos, A. P. Highly Luminescent Colloidal Nanoplates of Perovskite Cesium Lead Halide and Their Oriented Assemblies. *J. Am. Chem. Soc.* **2015**, *137*, 16008−16011.
(25) Milman, V.; Winkler, B.; White, J. A.; Pickard, C. J.; Payne, M. C.; Akhmatskaya, E. V.; Nobes, R. H. Electronic Structure, Properties, and Phase Stability of Inorganic Crystals: A Pseudopotential Plane-Wave Study. *Int. J. Quantum Chem.* **2000**, *77*, 895−910.
(26) Perdew, J. P.; Burke, K.; Ernzerhof, M. Generalized Gradient Approximation Made Simple. *Phys. Rev. Lett.* **1996**, *77*, 3865−3868.
(27) Inada, Y.; Orita, H. Efficiency of Numerical Basis Sets for Predicting the Binding Energies of Hydrogen Bonded Complexes: Evidence of Small Basis Set Superposition Error Compared to Gaussian Basis Sets. *J. Comput. Chem.* **2008**, *29*, 225−232.
(28) Delley, B. Hardness Conserving Semilocal Pseudopotentials. *Phys. Rev. B: Condens. Matter Mater. Phys.* **2002**, *66*, 155125.
(29) Diao, F. Y.; Tian, F. H.; Liang, W. S.; Feng, H. L.; Wang, Y. Q. Mechanistical Investigation on the Self-Enhanced Photocatalytic Activity of CuO/Cu_2O Hybrid Nanostructures by Density Functional Theory Calculations. *Phys. Chem. Chem. Phys.* **2016**, *18*, 27967−27975.
(30) Zhang, D. D.; Eaton, S. W.; Yu, Y.; Dou, L. T.; Yang, P. D. Solution-Phase Synthesis of Cesium Lead Halide Perovskite Nanowires. *J. Am. Chem. Soc.* **2015**, *137*, 9230−9233.
(31) Protesescu, L.; Yakunin, S.; Bodnarchuk, M. I.; Krieg, F.; Caputo, R.; Hendon, C. H.; Yang, R. X.; Walsh, A.; Kovalenko, M. V. Nanocrystals of Cesium Lead Halide Perovskites ($CsPbX_3$, X = Cl, Br, and I): Novel Optoelectronic Materials Showing Bright Emission with Wide Color Gamut. *Nano Lett.* **2015**, *15*, 3692−3696.
(32) Nivetha, K.; Madhuri, W. Structural, Spectral, Thermal, and Optical Studies of Stilbazolium Derivative Crystal: (E)-4-(3-hydroxy-4-methoxystyryl)-1-methyl pyridinium Iodide Monohydrate. *Opt. Laser Technol.* **2019**, *109*, 496−503.
(33) Chen, Y. H.; Smock, S. R.; Flintgruber, A. H.; Perras, F. A.; Brutchey, R. L.; Rossini, A. J. Surface Termination of $CsPbBr_3$ Perovskite Quantum Dots Determined by Solid-State NMR Spectroscopy. *J. Am. Chem. Soc.* **2020**, *142*, 6117−6127.
(34) Smock, S. R.; Williams, T. J.; Brutchey, R. L. Quantifying the Thermodynamics of Ligand Binding to $CsPbBr_3$ Quantum Dots. *Angew. Chem., Int. Ed.* **2018**, *57*, 11711−11715.
(35) Ye, X. C.; Chen, J.; Engel, M.; Millan, J. A.; Li, W. B.; Qi, L.; Xing, G. Z.; Collins, J. E.; Kagan, C. R.; Li, J.; Glotzer, S. C.; Murray, C. B. Competition of Shape and Interaction Patchiness for Self-Assembling Nanoplates. *Nat. Chem.* **2013**, *5*, 466−473.
(36) Mallavajula, R. K.; Archer, L. A. Nanocrystal Self-Assembly Assisted by Oriented Attachment. *Angew. Chem., Int. Ed.* **2011**, *50*, 578−580.
(37) Hines, M. A.; Scholes, G. D. Colloidal PbS Nanocrystals with Size-Tunable Near-Infrared Emission: Observation of Post-Synthesis Self-Narrowing of the Particle Size Distribution. *Adv. Mater.* **2003**, *15*, 1844−1849.
(38) Schliehe, C.; Juarez, B. H.; Pelletier, M.; Jander, S.; Greshnykh, D.; Nagel, M.; Meyer, A.; Foerster, S.; Kornowski, A.; Klinke, C.; Weller, H. Ultrathin PbS Sheets by Two-Dimensional Oriented Attachment. *Science* **2010**, *329*, 550−553.

https://doi.org/10.1021/acsami.1c12247
ACS Appl. Mater. Interfaces 2021, 13, 44777−44785